Analyst

ROYAL SOCIETY OF CHEMISTRY

PAPER

View Article Online
View Journal | View Issue

Cite this: *Analyst*, 2025, **150**, 1293

Tissue analysis by vibrational spectroscopy in Hirschsprung disease: feasibility and potential as a new intraoperative tool†

C. Combescot, [a] O. Piot, *[a] V. Untereiner, [b] A. Durlach[c,d] and F. Laconi[e]

Hirschsprung disease is a congenital anomaly characterised by an absence of innervation in the colon. The current diagnosis, which involves identifying the non-functional part of the colon through histological examination, is unsatisfactory. The objective of our study was to assess the potential of infrared spectroscopy as a label-free method to distinguish between functional and non-functional parts of the colon. Tissue samples from FFPE sections of Hirschsprung patients, taken from both functional and non-functional regions, were analysed by mid-infrared imaging. Colour-coded spectral images, reconstructed using multivariate data processing, were compared to the gold standard (hematoxylin–eosin–safran staining) to associate a specific spectral signature with each histological structure. Statistical analyses were also carried out to highlight infrared markers associated with Hirschsprung disease. The search for ganglion cells and cholinergic threads, the usual markers of the disease, was unsuccessful. However, our approach was efficient in differentiating between functional and non-functional parts of the colon by focussing on the muscularis. As such, vibrational spectroscopy can highlight biochemical differences that are not visible using standard histology. This proof-of-concept study suggests that vibrational spectroscopy is a candidate method for diagnosing Hirschsprung disease, paving the way for intraoperative application by assisting surgeons and histologists in delineating the pathological region.

Received 28th November 2024,
Accepted 9th February 2025

DOI: 10.1039/d4an01489h

rsc.li/analyst

Introduction

Hirschsprung disease (HD) is a congenital condition arising from disruption in the migration of neuroblasts from the neural crest during colon formation. It affects 1 in 5000 births, predominantly boys (ratio 4 : 1), and is associated with more than 12 genetic mutations.[1,2] In most cases, the diagnosis is clinically suspected within the first days of life, and a subsequent histological examination of rectal biopsies is the gold standard for confirming the diagnosis. Once the diagnosis is made, the treatment consists of surgical pull-through of the aganglionic tract. At that point, determining histologically the boundaries between the ganglionic/functional and aganglionic/non-functional colon segments involves confirming the presence of ganglion cells, which can be particularly challenging. Indeed, the identification of ganglionic cells necessitates an experienced pathologist with specific expertise. In addition, the tissue section examined may contain no ganglionic cells, even though the tissue is functional. In this case, it is necessary to redo the analysis to search for another part of the biopsy containing ganglionic cells. This extemporaneous examination, performed intraoperatively, takes approximately thirty minutes, during which the baby remains under general anaesthesia. Alternative techniques, such as enzymatic tests for detecting cholinergic networks, are too time-consuming for intraoperative use.

Aware of these challenges and limitations, we believe that introducing a new diagnostic tool could be valuable in the clinical management of this disease. Vibrational spectroscopy, an optical technique corresponding to two modalities, namely, Raman scattering and infrared (IR) absorption, appears to be a promising candidate tool, as it gives access to the overall biochemical composition of a sample in a single, label-free measurement. To our knowledge, the scientific literature includes only two studies related to the use of vibrational spectroscopy in HD.[3,4] These studies demonstrated the ability of Raman spectroscopy to obtain the spectral signature of ganglionic cells in a mouse model[3] and to detect the human enteric nervous system.[4] In our study, we focused our investigation on

[a]*Université de Reims Champagne-Ardenne, BioSpecT UR 7506, Reims, France. E-mail: olivier.piot@univ-reims.fr*
[b]*Université de Reims Champagne-Ardenne, URCATech, PICT, Reims, France*
[c]*Centre Hospitalier Universitaire de Reims, Hôpital Maison Blanche, Département de biopathologie, Reims, France*
[d]*Université de Reims Champagne-Ardenne, Inserm UMR-S 1250, P3Cell, Reims, France*
[e]*Centre Hospitalier Universitaire de Reims, Département de chirurgie pédiatrique, Reims, France*

† Electronic supplementary information (ESI) available. See DOI: https://doi.org/10.1039/d4an01489h

the mid-infrared imaging of tissue sections. This modality allows for the combination of chemical specificity with spatial information at the cellular scale without the need for extrinsic chemical treatments. The analysis relies on the non-destructive interaction between the infrared radiation and the matter, permitting the reuse of the sample for further additional analysis.[5] Combined with multivariate data processing, the approach turned out to be successful in the characterisation of cancerous[5–9] tissues by providing information on tumour heterogeneity, sometimes non accessible by conventional histology.

Vibrational spectroscopy is a new and promising candidate in the medical field, allowing diagnosis in a non-invasive or non-destructive way.[10–13] This technique can lead to the development of new approaches, such as the daily non-invasive monitoring of glycaemia.[12,13] Combined with a microscopic imaging device, this technique can provide complementary diagnostic markers to conventional histopathology, as demonstrated by studies on various diseases, such as inflammatory skin lesions,[11] lung fibrosis,[14] or cancerous malignancy.[15]

The objective of this proof-of-concept study was to assess the capacity of mid-infrared spectral imaging to identify HD tissues by distinguishing the functional part from the non-functional part of the colon. First, we evaluated the ability of IR imaging to detect the standard indicators of routine histological examination, namely, the ganglion cells at the level of Auerbach and Meissner plexus in functional tissue, and the cholinergic nets within the chorion of the mucosa of non-functional tissue. Second, our investigation focused on the muscularis of the colon; this structure showed no morphological alteration visible by standard histology.

Materials and methods

The methodology workflow is summarized in Fig. 1.

Sample collection and preparation

The study utilized tissue samples from colon macro-biopsies (n = 6) obtained from pull-through surgery, available in Formalin Fixed Paraffin-Embedded (FFPE) form, and from patients previously diagnosed with Hirschsprung disease (Table 1). Each patient contributed two samples, both from the functional and non-functional segments of the colon, resulting in a total of 12 samples for this proof-of-concept study.

For each sample, two successive 8 μm sections made with a microtome were used. The first section was deposited on a calcium fluoride (CaF_2) slide to carry out the acquisition by infrared imaging. The second adjacent section was placed on a glass slide for hematoxylin–eosin–safran (HES) staining, which marked the tissue structures. All stained tissue sections were digitalized using a VS120 digital scanner (Olympus, Tokyo, Japan).

All experiments were performed in accordance with French laws and approved by the local ethics committee (Comité d'éthique du Centre Hospitalier Universaire de Reims, France) under the approval number AC 2019-3408, after obtaining informed consent from the parents of every patient.

Analysis of spectral images acquired by infrared spectroscopy

Acquisition of the spectral images. The data were acquired with a Spotlight 400 IR microscope coupled with a Spectrum One spectrometer (PerkinElmer, Villebon-sur-Yvette, France) and using Spectrum Image software (Version R1.6.4.0394, PerkinElmer). Owing to the large size of the tissue samples and the limitation of the acquisition capacity of the IR equipment, the acquisitions were sectioned for each sample into several parts of equivalent size. Thus, a total of 63 images corresponding to the tissue samples were recorded. For each slide, one spectral image was also recorded on the paraffin without tissue for the numerical correction of paraffin interferences.

The spectral images were recorded with a spectral resolution of 4 cm^{-1}, 4 accumulations per pixel, over the spectral range of 4000–800 cm^{-1}. A pixel size of 6.25 × 6.25 μm^2 was chosen, offering spatial precision at the cellular scale.

In addition, polarisation-resolved infrared acquisitions were led with the same parameters by incorporating a polariser on the incident beam; images were collected with three orientations at 0°, 45° and 90° according to the sample orientation.

Data analysis. Data analyses were conducted with internally developed scripts written in Matlab (The Mathworks, Natick, MA) unless stated otherwise.

Spectral image pre-processing. First, an atmospheric correction was carried out to eliminate the absorption of environmental molecules, such as CO_2 and residual water vapor, using Spectrum Image software (PerkinElmer).

The spectral data were then corrected using Extended Multiplicative Signal Correction (EMSC), which simultaneously performed baseline correction, vector normalisation and digital neutralization of the paraffin interferences (S.D.1†). It also permits the removal of outlier spectra corresponding to noisy or weak intensity spectra. Normalisation uses a reference spectrum named the target. In the present study, two distinctive targets were used depending on the analysis made. Target #1 was the average of the spectra of a complete tissue (mucosa, sub-mucosa, muscularis and nerve plexus) and was used for the spectral analysis at the complete tissue level. For analysis focused on the muscularis structure, a second target, target #2, was used; it corresponded to the mean of spectra extracted from a reduced zone containing only the muscularis and parts of the nerve plexus. To determine these targets, we considered the sample from patient #1 for the quality of the section (S. D.1†). For this pre-processing step, the spectral range was reduced to the 1800–900 cm^{-1} fingerprint region, containing the most vibrational information in biological samples.

Construction of pseudo-colour spectral images using K-means clustering. The pre-processed spectra were then submitted to unsupervised clustering to partition data according to their spectral similarity. Here, K-means (KM) clustering was used to separate the spectra into a chosen number of classes called clusters and by grouping the most similar spectra

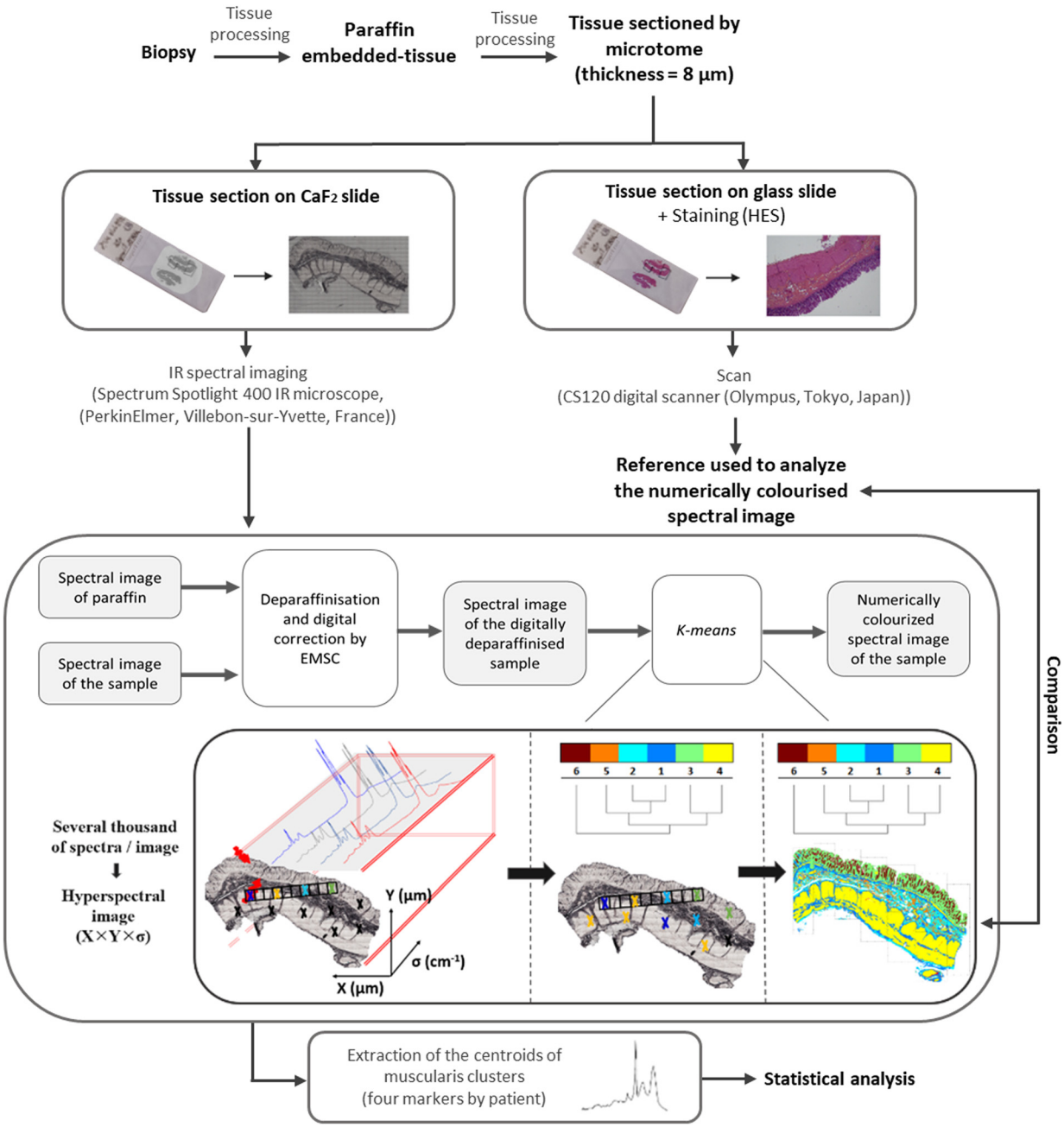

Fig. 1 Experimental approach for the acquisition and processing of a spectral image from a paraffin-embedded histological section acquired by FTIR. EMSC: extended multiplicative signal correction; KM: K-means.

Table 1 Summary of the patients' data

Patient number	Age	Sex	Extension of the aganglionosis
1	6 months	F	Sigmoid
2	6 months	M	Sigmoid
3	4 months	F	Sigmoid
4	6 months	F	Sigmoid
5	3 months	M	Sigmoid
6	1 month	M	Sigmoid

within specific clusters; a centroid associated with each cluster represents the spectral profile of this cluster. The results can be visualized in the form of a pseudo-colour image in which each cluster is associated with a colour. A dendrogram showing the relative spectral proximity of the centroids is also constructed. It should be noted that the colours are randomly assigned to the clusters from one KM clustering to another, so there is no correspondence between the colours of the two distinct clusterings. Pseudo-colour K-means images were subsequently compared with HES staining on adjacent sections to attribute the clusters to specific histological structures.

Identification of discriminant vibrations associated with the Hirschsprung condition. Owing to differences in size between the samples, the number of spectral images was not the same for every section. Thus, for better representativeness in the statistical analysis, four areas of the same size containing the muscularis were extracted from the spectral images of each tissue section. Each area was submitted to individual KM clustering. Then, the most discriminative wavenumbers between functional and non-functional tissues were searched from the spectral centroids of the KM clusters corresponding to the muscularis structures.

An inferential non-parametric univariate analysis was carried out for each feature of the spectral data using a Kruskal–Wallis test, followed by the calculation of the *p*-value using a χ^2 test, with 95% and 99% thresholds.

Results

Definition of histological structures of interest

In HD, the functional or non-functional area of the colon is characterised respectively by the presence or absence of ganglion cells and is validated by histopathological examination of HES-stained tissue samples observed under a microscope (Fig. 2). The tissue is deemed functional if the ganglion cells are present, or non-functional otherwise. Thus, confirming the presence of ganglion cells is the gold standard for classifying a sample as healthy, ruling out a diagnosis of disease.

Another way to validate the HD diagnosis is the presence of a cholinergic net in the mucosa and submucosa of the non-functional area.[16] This second marker has two flaws, making it difficult to use as a reliable and reproducible gold standard.

The first is that the presence of a cholinergic net can only be verified in fresh or frozen tissues by treating the tissue with acetylcholinesterase (AchE). Our study relied on paraffin-embedded tissues, and it was not possible to determine the presence and quantity of cholinergic nets by AchE staining. The second is the density of these nets, which varies among patients, with some exhibiting dense nets, whereas others have nearly non-existent ones.[17] However, some of the non-functional tissues presented large and visible hypertrophied nerve trunks with HES staining, which is known to be correlated with the presence of cholinergic nets. We tried to search for a spectral signature for the hypertrophied nerve trunks or for the cholinergic nets on the FFPE tissues, but we were not able to isolate any specific spectral signature (data not shown). Therefore, the question of the cholinergic net is still pending, and more tests should be carried out on fresh or frozen tissue.

Characterisation of the HD tissues using IR microimaging

This part of the analysis focused on the myenteric plexus of confirmed functional tissues because the ganglion cells were

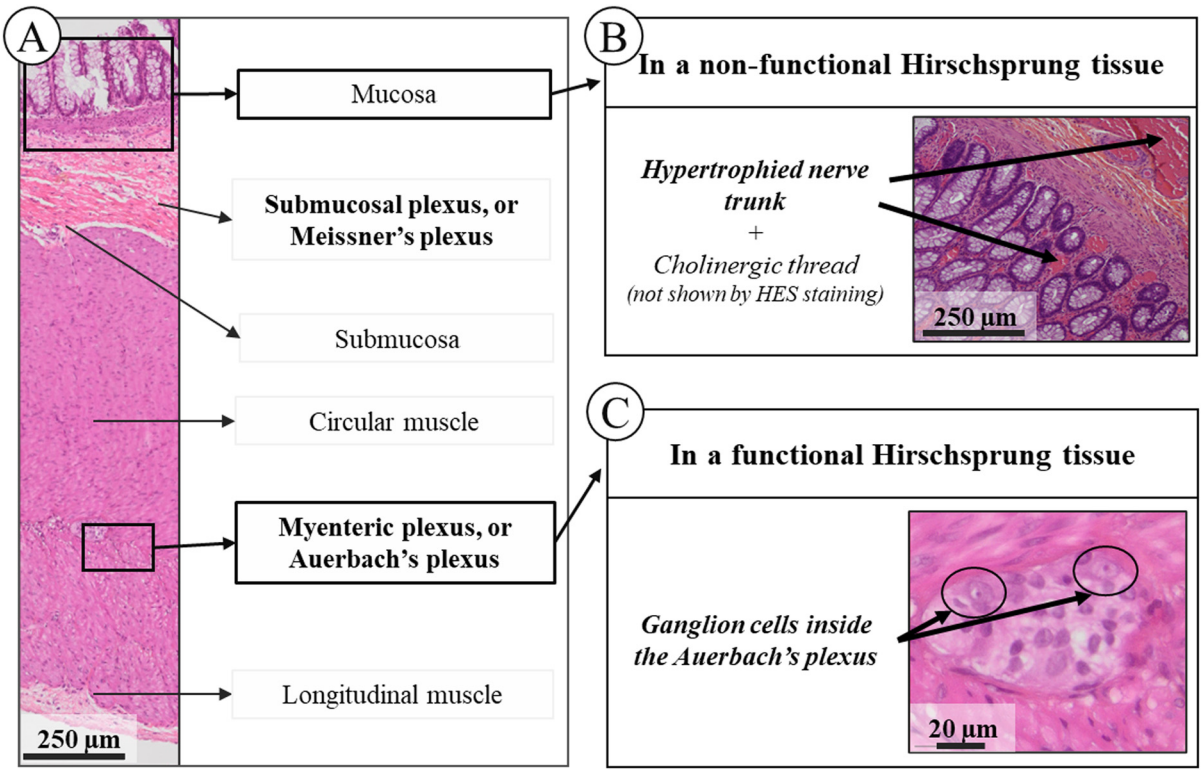

Fig. 2 Simplified anatomy of the colon and corresponding HES-stained slide. (A) Colon histology and structure in an HES-stained section. (B) and (C) Stained sections showing, respectively, hypertrophied nerve trunks within the mucosa and ganglion cells within the Auerbach plexus. The HES-stained slides were scanned at a magnification of ×40.

easier to find compared to the submucosal plexus. First, the tissue sections, including the mucosa, sub-mucosa and muscularis, were analysed by infrared to find a specific spectral signature of the ganglion cells.

The KM analysis on spectral images did not reveal a specific cluster associated with the ganglionic cells even if the number of clusters was increased. However, the submucosa heterogeneity was highlighted by multiplying clusters in this structure but not in the plexus. Then, the analysis focused on a reduced area containing only the myenteric plexus and the surrounding muscularis (S.D 2†). Despite increasing up to fifteen clusters, we were not able to find a signal specific to the ganglion cells (S.D 2†). Although a specific spectral signature for ganglion cells was identified in both IR and Raman micro-spectroscopy in previous studies,[18,19] we were not able to locate them using IR microimaging with a pixel size of 6.25 × 6.25 μm^2. This could be attributed to the size of the cells averaging 20 μm. Thus, if a ganglion cell was between two pixels, its spectral signal would be mixed with that of the plexus. This hypothesis is reinforced by the fact that other teams were able to obtain an IR spectral signature of the ganglion using a pixel size of 2.6 × 2.6 μm^2.[18] Moreover, although two adjacent thin sections were used for infrared imaging and HES staining, it could be possible that one section contained cells whereas the other did not.

Comparison of infrared imaging of healthy and pathological tissue

Considering that the ganglion cells were undetectable with the spatial resolution of our equipment, our analysis was then focused on other tissue structures of functional and non-functional parts of the colon samples from patients with Hirschsprung disease.

Although standard histology did not show any morphological differences, infrared imaging permitted highlighting differences at the level of the muscularis between the non-functional and functional segments in HD tissues. Fig. 3 shows the KM results obtained for a representative case. Tests were conducted to find the minimum number of clusters required to separate the HD and healthy muscularis segments. A difference in the cluster number was observed among the patients: for patients #1, #2, and #3, 7 clusters were found to be necessary, while patient #4 required 9 clusters, and patients #5 and #6 required 10 clusters (data not shown). These disparities can be explained by high inter-patient variability in the submucosa and mucosa. These spectral variabilities in the mucosa and sub-mucosa are not attributed to the disease, as the clusters are present both in the functional and non-functional segments of the same patient.

At the methodological level, this disparity constitutes a limitation in the automation of the approach because the operator must intervene to adjust the parameters for each case. To avoid interferences originating from the mucosa and submucosa, the solution is to use spectral images containing only the muscularis and the plexus of the tissue. It was then possible to discriminate for all cases between the non-functional and functional parts of the colon with a cluster number fixed to 4 (S.D 3†).

Based on these positive results, the last step of our study was to identify wavenumbers that can be considered spectral markers to discriminate between the functional and non-functional segments of the tissue. Thus, the centroids corresponding to the muscularis extracted from 4 distinctive spectral images for each patient and each condition were statistically compared through a Kruskal–Wallis test; thus, 24 spectra representatives of each of the 2 conditions were considered. For a given wavenumber, a p-value over the significance level (here 0.05 or 0.01) reflects a difference in intensity between the two conditions. The wavenumbers associated with significant differences are shown in Fig. 4. The mean spectra and standard deviations are also displayed to better visualize the position of the spectral discriminant differences. From the scientific literature, we were able to assign the majority of these most discriminative wavenumbers mainly to protein, RNA and phospholipid contents. The wavenumbers around 1720 cm^{-1} are associated with C=O stretching found in lipid esters.[20,21] The 1540 cm^{-1} vibration is associated with the Amide II band, resulting from N—H bending and C—N stretching modes in proteins.[20–23] The vibrations at 1428–1444 cm^{-1} can correspond to both CH_2 bending in lipids and CH_3 bending in proteins.[20,21] The spectral range 1386–1398 cm^{-1} is associated with CH_3 bending vibrations present in fatty acids and phospholipids,[20] and the wavenumbers at 1320–1330 cm^{-1} correspond to C—O stretching vibrations of carbohydates.[24] The wavenumbers between 1232 and 1250 cm^{-1} can contribute to the Amide III band, arising from C—N stretching and N—H bending modes in proteins and PO_2^- stretching vibration of RNA,[20,21] while the wavenumbers between 1268 and 1280 cm^{-1} are assigned to PO_2^- stretching vibration of phospholipids.[21,22] The wavenumber around 1110 cm^{-1} can be associated with stretching vibration of the C—O ester-groups.[21] The 1028 and 1154 cm^{-1} wavenumbers can correspond to C—O—H and C—O—C bending vibrations of glycogen.[20] The set of vibrations located between 900 and 974 cm^{-1} are likely to be associated with the C—N—C stretching in RNA and phospholipids, or with C—O—C deformations in carbohydtates.[22,24] Since the tissues were paraffined, the vibrations associated with the lipid contents correspond to components of the cell membrane. The discriminative wavenumbers implicated suggest several biochemical changes in the tissues, most likely an alteration in the protein content and structure. But it could also be due to a difference in the molecular components of muscle cells, the absence of ganglion cells inducing a modification in the expression of muscle cells, and particularly those of the outer tunic. This hypothesis is supported by the numerous genetic mutations as described in the literature in Hirschsprung patients.[2] Moreover, the heterogeneity between the patients must be considered. The most discriminative wavenumbers varied between patients, and this statistical analysis permitted to highlight the most common variations across all patients.

The discriminant vibrations identified previously can be considered spectroscopic markers of HD and permit biochemi-

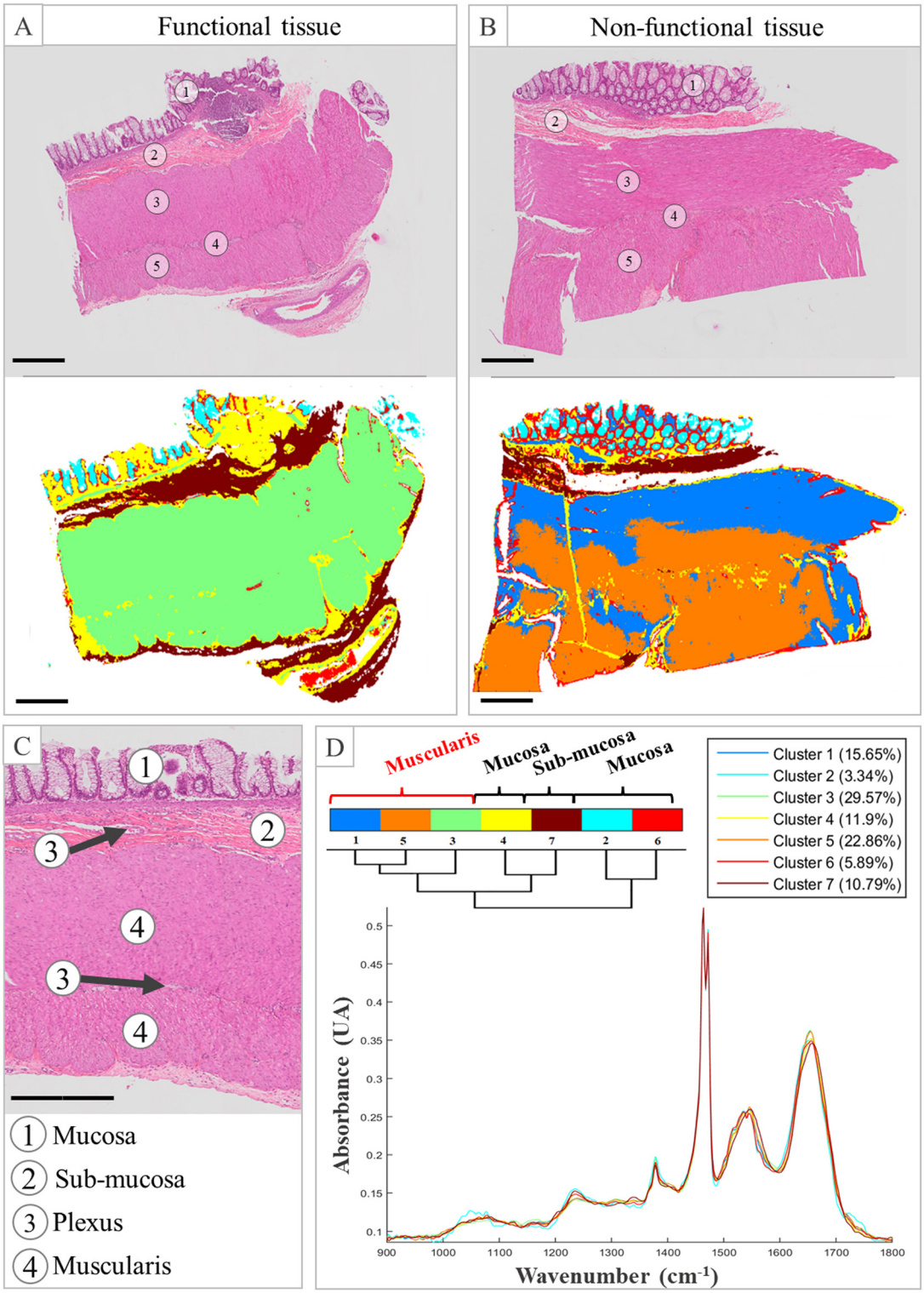

Fig. 3 KM clustering of ganglionic and aganglionic parts of Hirschsprung patient samples. (A) and (B) HES-stained tissue and common KM with 7 clusters of functional and non-functional (ganglionic) tissue (×40), respectively. (C) Anatomy of the colon (×40). (D) Dendrogram and centroid of common KM. The scale bar represents 500 μm. The HES-stained slides were scanned at a magnification of ×40.

cal interpretation of the spectral changes observed. In the case of the muscularis structures, it is also questionable whether there is a relationship between the spectral features and the muscle structure and/or organization. Indeed, the muscle fibres are differently oriented between the inner tunic and the outer tunic of the colon. Possibly, analysing the fibre orien-

A

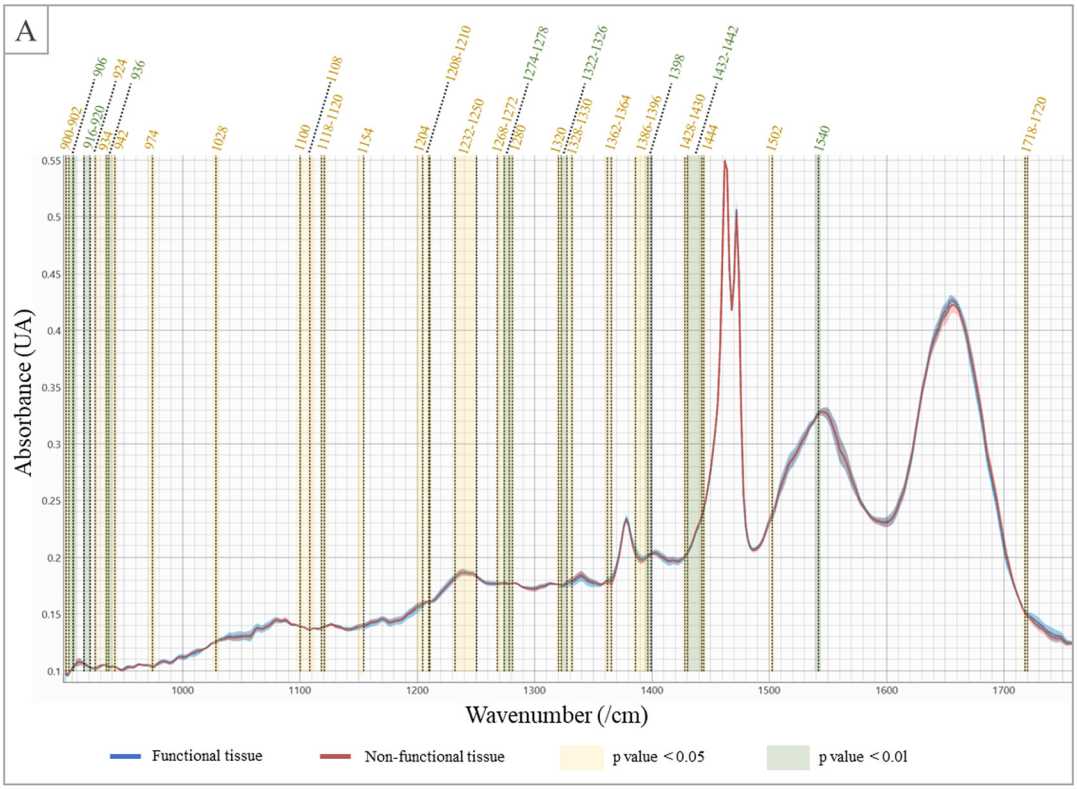

B

	900	902	906	916	918	920	924	934	936	942	974	1028	1100
H VALUE	5,8202	5,5255	12,4324	12,4324	12,8724	14,2385	3,9184	4,2517	7,2963	4,5106	4,1671	4,7772	4,0833
p value	0,0158	0,0187	0,0004	0,0004	0,0003	0,0002	0,0478	0,0392	0,0069	0,0337	0,0412	0,0288	0,0433

	1108	1118	1120	1154	1204	1208	1210	1232	1234	1236	1238	1240	1242
H VALUE	4,6875	4,2517	5,5255	4,5986	4,0833	5,1446	5,0979	4,8678	5,6229	6,2249	6,1224	5,7211	4,4235
p value	0,0304	0,0392	0,0187	0,0320	0,0433	0,0233	0,0240	0,0274	0,0177	0,0126	0,0133	0,0168	0,0354

	1246	1248	1250	1268	1270	1272	1274	1276	1278	1280	1320	1322	1324
H VALUE	4,3372	4,5106	4,0004	4,5986	4,0004	4,9592	9,5663	10,2147	10,3469	4,7772	5,7211	13,9290	11,1582
p value	0,0373	0,0337	0,0455	0,0320	0,0455	0,0260	0,0020	0,0014	0,0013	0,0288	0,0168	0,0002	0,0008

	1326	1328	1330	1362	1364	1386	1388	1390	1392	1394	1396	1398	1428
H VALUE	6,7500	5,3333	4,5106	6,0208	4,1671	3,9184	6,3282	6,1224	5,4290	6,0208	5,9201	7,5208	4,4235
p value	0,0094	0,0209	0,0337	0,0141	0,0412	0,0478	0,0119	0,0133	0,0198	0,0141	0,0150	0,0061	0,0354

	1430	1432	1434	1436	1438	1440	1442	1444	1502	1540	1718	1720
H VALUE	4,8678	10,2807	14,3946	9,9528	9,2501	12,1433	11,7160	6,3282	4,2517	8,4528	4,0004	3,9184
p value	0,0274	0,0013	0,0001	0,0016	0,0024	0,0005	0,0006	0,0119	0,0392	0,0036	0,0455	0,0478

Fig. 4 Mean spectra and standard deviations of the functional and non-functional parts of the colon (shown in blue and red, respectively), with the statistically different wavenumbers identified from a Kruskal–Wallis test and a χ^2 test. (A) The areas where the peak absorbances are significantly different are colored in yellow (95%) and green (99%). (B) The H values calculated from the rank of the Kruskal–Wallis test and the *p*-value are reported in the table.

tation could be a supplementary indicator in HD diagnosis. Following this hypothesis, our idea was to check whether polarisation-resolved infrared imaging would enhance spectral differences within the muscularis when compared to non-polarised measurements. For this test, a healthy segment was analysed by changing the polarisation of the incident infrared beam. Previous studies conducted in our laboratory revealed the interest in polarising the infrared incident beam to probe the orientation of biological macromolecules, such as type I collagen.[25] The polarisation measurements were carried out by orientating the electric field of the incident beam at a precise angle in relation to the structures of the tissue (aligned horizontally as shown in Fig. 1A and B). The polarised measurements at 0°, 45° and 90° were compared with each other and with non-polarised measurements through a common KM clustering. From this experiment, it appeared that the polarisation of the infrared incident beam had a negligible effect on the spectral signatures of the tissue structures (Fig. 5). Indeed, common KM clustering was carried out on both functional and pathological parts of an HD specimen for three con-

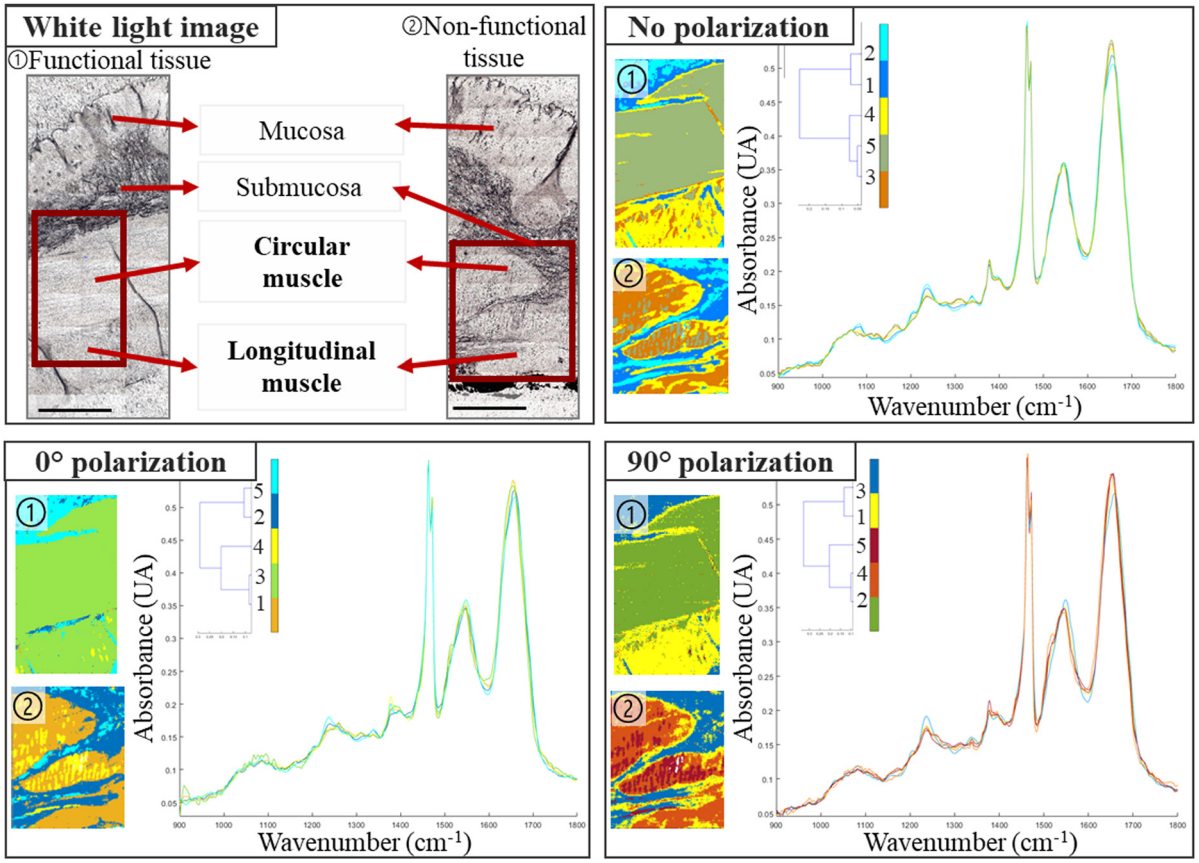

Fig. 5 Analyses of the orientation of the fibres on the spectral image of the functional (①) and non-functional (②) parts of the colon of the same patient with KM clustering. Each spectral image is a cropped part of the whole tissue, composed of the submucosa, the circular muscle and the longitudinal muscle. Five clusters were used for each pair with a 0° and 90° polariser and without a polariser. The scale bar represents 500 μm.

ditions: without polarisation, and with polarisation angles of 0° and 90° according to the tissue orientation on the motorized plate of the instrument. Five clusters were chosen for this KM clustering. The overall spatial distribution of the clusters and the respective spectral distances between their centroids, as can be assessed by the dendrograms, were similar independently to the polarisation condition. In particular, the Amide I-to-Amide II intensity ratio, previously shown to be affected by the polarisation,[25] appeared here stable. This experiment demonstrated that the tissue components of the colon are insensitive to the orientation of the electric field of the infrared radiation and that using polarisation does not enhance the spectral differences between the inner and outer tunics.

Our results demonstrated that IR imaging can distinguish between functional and non-functional parts of the colon of Hirschsprung patients; however, the main study's limitation is the small number of patients (n = 6). Because Hirschsprung disease is a rare disease, we obtained samples from only 6 patients after obtaining their consent, in collaboration with local medical doctors. An expanded patient cohort relying on multicentric sampling would enhance result reliability and permit the creation of a predictive model using supervised classification methods for the implementation of an automated diagnostic tool. Additionally, there are case reports where samples containing ganglion cells are found to be non-functional after surgery, necessitating further intervention. This region, known as the transitional zone, poses significant risks when performing an anastomosis (Transition Zone Anastomosis – TZA), potentially leading to serious complications and adversely affecting patient outcomes.[26,27] Exploring the spectral characteristics of the TZA seems necessary because there are no existing methods to differentiate this part from the functional area of the colon. This could offer valuable insights because our approach is not based on the presence or absence of the cells. Addressing this clinical question may aid in defining surgical excision limits. However, this exploration requires the inclusion of new patients present with this complication because none of the patients included in the present study had this complication.

Conclusions

Infrared microimaging permits the differentiation of the functional and non-functional parts by analysing the muscularis structure. Our proof of concept paves the way for developing

an automated tool complementary to the standard histological technique to assist in the diagnosis of Hirschsprung disease.

Author contributions

O. Piot, F. Laconi contributed to the conception, design and drafting of the paper. C. Combescot performed the acquisitions and curation of the data, computational experiments, and data analysis. F. Laconi performed the surgeries from where the samples were taken. A. Durlach confirmed the histological composition of the sample and the patient's disease and selected the tissues used for this study. V. Untereiner and O. Piot supervised the acquisition and validated the data analysis of the study. All authors reviewed the final version and approved the submission.

Data availability

Data for this article are available at the SSDS of the University of Reims Champagne-Ardenne at **https://ssds-cloud.univ-reims.fr/index.php/s/LsGmQZeBy6WQoYD**. As per the University's policy, sharing links have a limited lifespan; after expiration, the link will be reactivated upon request. However, personal data collected from human participants, as described in [Table 1], are not available due to confidentiality reasons.

Conflicts of interest

There are no conflicts to declare.

Acknowledgements

The authors thank the URCATech, PICT-IBiSA platform of the University of Reims Champagne-Ardenne for spectroscopy facilities. This work has been made within the framework of the Graduate School NANO-PHOT (École Universitaire de Recherche, PIA3, contract ANR-18-EURE-0013). The authors also thank the biobank of the CHU of Reims (Département de Biopathologie) for the biopsies. The authors would also like to thank Dr Cyril GOBINET, from BioSpecT UR 7506 (Reims, France), for his help and insight with the statistical analysis.

References

1 R. O. Heuckeroth, *Nat. Rev. Gastroenterol. Hepatol.*, 2018, **15**, 152–167.
2 C. S. Tang, A. Karim, Y. Zhong, P. H. Chung and P. K. Tam, *Pediatr. Surg. Int.*, 2023, **39**, 104.
3 M. A. Soares de Oliveira, L. Galganski, S. Stokes, C.-W. Chang, C. D. Pivetti, B. Zhang, K. E. Matsukuma, P. Saadai and J. W. Chan, *Sci. Rep.*, 2021, **11**, 1398.
4 K. Ogawa, Y. Oshima, T. Etoh, Y. Kaisyakuji, M. Tojigamori, Y. Ohno, N. Shiraishi and M. Inomata, *J. Pediatr. Surg.*, 2021, **56**, 1150–1156.
5 K.-Y. Su and W.-L. Lee, *Cancers*, 2020, **12**, 115.
6 J. Nallala, M.-D. Diebold, C. Gobinet, O. Bouché, G. D. Sockalingum, O. Piot and M. Manfait, *Analyst*, 2014, **139**, 4005–4015.
7 G. M. Magno, G. E. Lotilla, E. R. Ambrosio, F. L. Nagera, M. I. Grino, M. R. Castro, J. A. Millan, J. A. Manzano, R. E. Tiongco and P. M. Albano, *Asian Pac. J. Cancer Prev.*, 2024, **25**, 1487–1495.
8 L. A. Courtenay, I. Barbero-García, S. Martínez-Lastras, S. Del Pozo, M. Corral de la Calle, A. Garrido, D. Guerrero-Sevilla, D. Hernandez-Lopez and D. González-Aguilera, *PLoS One*, 2024, **19**, e0300400.
9 M. Féré, C. Gobinet, L. H. Liu, A. Beljebbar, V. Untereiner, D. Gheldof, M. Chollat, J. Klossa, B. Chatelain and O. Piot, *Anal. Bioanal. Chem.*, 2020, **412**, 949–962.
10 Z. Fan, J. Zhang, C. Ma, B. Cong and P. Huang, *Forensic Sci., Med., Pathol.*, 2024, DOI: **10.1007/s12024-024-00866-9**.
11 D. Sebiskveradze, B. Bertino, V. Gaydou, A.-S. Dugaret, M. Roquet, D. E. Zugaj, J. J. Voegel, P. Jeannesson, M. Manfait and O. Piot, *J. Biophotonics*, 2018, **11**, e201700380.
12 J. W. Kang, Y. S. Park, H. Chang, W. Lee, S. P. Singh, W. Choi, L. H. Galindo, R. R. Dasari, S. H. Nam, J. Park and P. T. C. So, *Sci. Adv.*, 2020, **6**, eaay5206.
13 J. Liu, J. Chu, J. Xu, Z. Zhang and S. Wang, *Spectrochim. Acta, Part A*, 2025, **329**, 125584.
14 V. Suryadevara, S. S. Nazeer, H. Sreedhar, O. Adelaja, A. Kajdacsy-Balla, V. Natarajan and M. J. Walsh, *Biomed. Opt. Express*, 2020, **11**, 3996–4007.
15 M. Diem, A. Mazur, K. Lenau, J. Schubert, B. Bird, M. Miljković, C. Krafft and J. Popp, *J. Biophotonics*, 2013, **6**, 855–886.
16 R. K. Agrawal, N. Kakkar, R. K. Vasishta, V. Kumari, R. Samujh and K. L. N. Rao, *Diagn. Pathol.*, 2015, **10**, 208.
17 A. K. Braczynski, S. Gfroerer, R. Beschorner, P. N. Harter, P. Baumgarten, U. Rolle and M. Mittelbronn, *BMC Pediatr.*, 2020, **20**, 399.
18 C. Krafft, D. Codrich, G. Pelizzo and V. Sergo, *J. Biophotonics*, 2008, **1**, 154–169.
19 M. A. Soares De Oliveira, L. Galganski, S. Stokes, C.-W. Chang, C. D. Pivetti, B. Zhang, K. E. Matsukuma, P. Saadai and J. W. Chan, *Sci. Rep.*, 2021, **11**, 1398.
20 B. Zupančič, N. Umek, C. K. Ugwoke, E. Cvetko, S. Horvat and J. Grdadolnik, *Int. J. Mol. Sci.*, 2022, **23**, 12498.
21 B. Zupančič, C. K. Ugwoke, M. E. A. Abdelmonaem, A. Alibegović, E. Cvetko, J. Grdadolnik, A. Šerbec and N. Umek, *Front. Endocrinol.*, 2023, **14**, 1308373.
22 O. Bozkurt, M. Severcan and F. Severcan, *Analyst*, 2010, **135**, 3110–3119.
23 S. Magalhães, I. Almeida, F. Martins, F. Camões, A. R. Soares, B. J. Goodfellow, S. Rebelo and A. Nunes, *Molecules*, 2021, **26**, 6410.

24 J. Lopes, M. Correia, I. Martins, A. G. Henriques, I. Delgadillo, O. da Cruz E Silva and A. Nunes, *J. Alzheimers Dis.*, 2016, **53(3)**, 801–812.
25 C. Eklouh-Molinier, T. Happillon, N. Bouland, C. Fichel, M.-D. Diébold, J.-F. Angiboust, M. Manfait, S. Brassart-Pasco and O. Piot, *Analyst*, 2015, **140**, 6260–6268.
26 F. Chen, X. Wei, X. Chen, L. Xiang and J. Feng, *Front. Pediatr.*, 2021, **9**, 600316.
27 K. Taghavi, L. Goddard, S. M. Evans, A. Hobson, S. W. Beasley, S. Sankaran, A. Kukkady, J. Stevenson and M. D. Stringer, *Aust. N. Z. J. Surg.*, 2020, **90**, 1037–1040.